SCIENCE CHINA Materials ARTICLES

mater.scichina.com link.springer.com

Published online 27 March 2020 | https://doi.org/10.1007/s40843-019-1265-9
Sci China Mater 2020, 63(6): 1065–1075

Aligned monolayer MoS_2 ribbons growth on sapphire substrate *via* NaOH-assisted chemical vapor deposition

Shike Hu[1,2†], Jing Li[1,2†], Xiaoyi Zhan[1,2], Shuang Wang[1,2], Longbiao Lei[1,2], Yijian Liang[1,2], He Kang[1,2], Yanhui Zhang[1], Zhiying Chen[1], Yanping Sui[1], Da Jiang[1], Guanghui Yu[1,2*], Songang Peng[3], Zhi Jin[3] and Xinyu Liu[3]

ABSTRACT **This study reports the growth of aligned monolayer molybdenum disulfide (MoS_2) ribbons on a sapphire substrate *via* NaOH-assisted chemical vapor deposition. The length of MoS_2 ribbon is up to 400 μm. The MoS_2 ribbon has excellent single crystal properties, a carrier mobility of ~ 150 $cm^2 V^{-1} s^{-1}$, and a optical response of 103 mA W^{-1} at a wavelength of 550 nm. The growth model of MoS_2 ribbons was given. NaOH reacts with MoO_3 to form sodium molybdate droplets, which increase the fluidity of the molybdenum source on the substrate, realizing the vapor–liquid–solid growth of MoS_2 on sapphire. The monolayer MoS_2 ribbons have two kinds of arrangements on the sapphire substrate, one is the oriented growth affected by the interlayer van der Waals force and the lattice, and the other is the aligned growth constrained by the sapphire step. Our results promote the basic research and device applications of MoS_2, and introduce a new way of synthesizing other one dimensional (1D) and 2D nanostructures.**

Keywords: MoS_2, aligned ribbons, vapor-liquid-solid, step, epitaxy

INTRODUCTION

Two dimensional (2D) transition metal dichalcogenides (TMDCs) have received attention because of their unique properties [1–3]. Molybdenum disulfide (MoS_2) is a typical TMDC with the atomic layer thickness and excellent optoelectronic performance. It has huge potential applications in optoelectronic devices, flexible electronic devices, transistors, and sensors [4–7]. Many efforts have been made on the controllable preparation of MoS_2 films, including changing the source mode, growth mode, substrate selection and introducing precursor promoters [8–10]. The controllable synthesis of MoS_2 opens up a prospect for exploring its basic physical properties and practical device applications [11–14]. To date, the control of MoS_2 size, morphology, number of layers, and crystal orientation still remains a challenge.

Chemical vapor deposition (CVD) is the universal route for preparing many TMDCs and other 2D materials [15–18]. The microscopic mechanism of CVD is that the precursor of gas/vapor phase nucleates and then regenerates into films on the substrate [19]. A new molten salt-assisted CVD method for growing TMDCs has recently attracted attention [20–25]. The introduction of alkali metal promoter can effectively enhance the lateral growth of the film, making it a unique method for obtaining large-size single crystals. Zhou *et al.* [26] reported that the molten salt-assisted CVD can be applied for the synthesis of a wide variety of 2D TMDCs. The main mechanism is that the introduction of salt decreases the melting point of reactants and promotes the formation of intermediate products, thereby increasing the growth speed. Yang *et al.* [27] found that the adsorption of Na^+ on the edge of MoS_2 domains decreased the energy barrier and thus increased the growth rate. In addition to promoting lateral growth ability, the introduction of sodium-containing salts greatly affects the morphology and

[1] State Key Laboratory of Functional Materials for Informatics, Shanghai Institute of Microsystem and Information Technology, Chinese Academy of Sciences, Shanghai 200050, China
[2] Center of Materials Science and Optoelectronics Engineering, University of Chinese Academy of Sciences, Beijing 100049, China
[3] Microwave Devices and Integrated Circuits Department, Institute of Microelectronics, Chinese Academy of Sciences, Beijing 100029, China
† These authors contributed equally to this work.
* Corresponding author (email: ghyu@mail.sim.ac.cn)

crystal orientation of MoS_2. Li *et al.* [28] obtained highly crystalline anisotropic monolayer MoS_2 nanoribbons on NaCl crystal substrates or MoS_2 continuous films. The presence of NaCl causes the original vapor–solid–solid (VSS) growth mode to transfer to the vapor–liquid–solid (VLS) growth mode. In addition, Chen *et al.* [29] obtained oriented $MoSe_2$ nanoribbons on monolayer $MoSe_2$ films and randomly arranged $MoSe_2$ nanoribbons on the mica with the assistance of NaCl. The width of the $MoSe_2$ nanoribbons can be adjusted from a few hundred nanometers to a few microns by tuning the growth temperature. Although the studies on MoS_2 and $MoSe_2$ nanoribbons have been reported, large-area, uniform, highly crystalline, and highly aligned MoS_2 ribbons are not directly obtained on dielectric substrates, hindering the application of MoS_2 ribbons in electronic and optoelectronic devices.

Herein, we report the growth of monolayer MoS_2 ribbons *via* NaOH-assisted CVD on sapphire substrates, which is a typical VLS growth mode (NaOH reacts with MoO_3 at high temperature and forms sodium molybdate droplets, which increase the mobility of the source on the substrate). We found that the amount of the introduced NaOH considerably affects the MoS_2 morphology and orientation distribution on the sapphire substrate. The length of aligned MoS_2 ribbons can reach up to 400 μm. This study provides a novel idea for preparing 2D TMDCs ribbon and promotes the application of TMDCs in high-performance devices.

EXPERIMENTAL SECTION

CVD growth of monolayer MoS_2

The S, MoO_3 powders mixed with the NaOH crystal and the substrate were placed in different heating zones in the furnace. The temperature of S, MoO_3, and the substrate were 180, 700, and 850°C, respectively. Moreover, the carrier gas was 100 sccm of Ar, and the pressure was maintained at approximately 15 kPa during the growth. The furnace rapidly cooled down to room temperature after 8 min of growth.

Characterizations

A scanning electron microscope (SEM, Zeiss Super 55) with a voltage of 1.5 kV was used to collect SEM images. Raman spectra were detected by a Thermo-Fisher DXR 532 nm Filter Micro-Raman system. Atomic force microscopy (AFM, Bruker Dimension Icon) was conducted by tapping mode in air. Photoluminescence (PL) spectroscopy was performed using a WITec alpha300RS spectrometer equipped with a 532 nm excited line. PL spectra were collected under a laser power of ~0.433 mW with the integration time of ~10 s. The energies of the PL maps were centered at the A-exciton peak. Surface analysis of the catalysts was performed by X-ragy photoelectron spectroscopy (XPS) using a Thermo-Fischer ESCALAB 250X photoelectron spectrometer. The spectra were recorded using monochromated X-ray irradiation Al Kα ($h\nu$=1486.7 eV) and a 180° double-focusing hemispherical analyzer with a six-channel detector. In the XPS measurements, the binding energies of the photoemission spectra were calibrated against the C 1s peak of adventitious carbon at 284.8 eV. A JEM-2100F field emission transmission electron microscope (TEM) with an acceleration voltage of 200 kV was used to collect high resolution TEM (HRTEM) images.

Fabrication of MoS_2 Hall devices

The standard electron beam lithography was performed to fabricate the Hall bar structure device (10 nm Ti/100 nm Au), with sapphire as the substrate, the width of the MoS_2 channel of 1.5 μm, and the length of the MoS_2 channel of 2.2 μm.

Fabrication of MoS_2 photodetector devices

The physical vapor deposition (thermal evaporation) was conducted to fabricate the device with a 150 μm-wide active channel and a length of 2 mm. The substrate was sapphire, and 50 nm-thick Au layers were coated on the surface as a pair of electrodes.

RESULTS AND DISSCUSION

Characterizations of aligned MoS_2 ribbons

The growth of monolayer MoS_2 ribbons was achieved *via* the NaOH-assisted CVD. Highly polished and clean *C*-plane sapphire, with a miscut orientation of *C*-axis [0001] and tiled *M*-axis of 0.2°±0.1°, was selected as the substrate. The setup, a three-temperature zone CVD tube furnace, was used for the CVD growth as illustrated in Fig. 1a. A typical optical image of MoS_2 ribbons with certain orientation on sapphire is shown in Fig. 1b. The widths of MoS_2 ribbons are several microns, and the lengths are approximately 80 μm. Fig. 1c shows the SEM image of the MoS_2 ribbons, and the independent ribbons appear as parallel. Fig. 1d shows the AFM topography image of the synthesized MoS_2 ribbon. The synthesized MoS_2 ribbon is monolayer with a thickness of 0.95 nm. The XPS spectra further proved those ribbons are MoS_2. As shown in Fig. 1e, Mo 3d has two peaks at 229.5 and

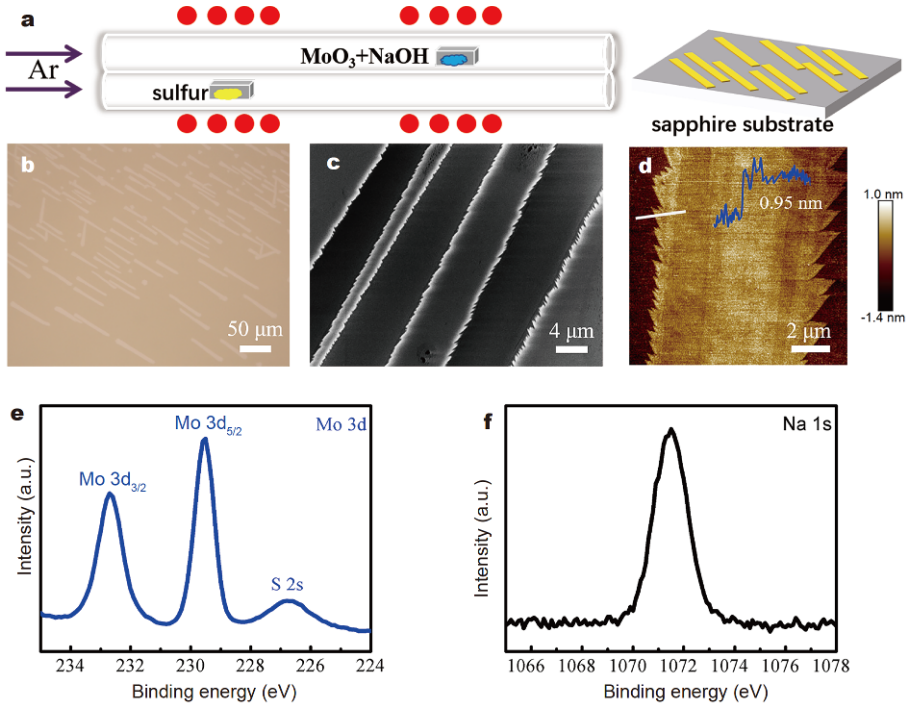

Figure 1 (a) Schematic illustration of CVD setup for MoS_2 ribbon growth. (b) Typical optical image of MoS_2 ribbons grown with the assistance of NaOH. (c) SEM image of the MoS_2 ribbons. (d) AFM topography image of monolayer MoS_2 ribbon. The inset is the height profile plotted alone a white line. (e) XPS spectra of the Mo 3d and S 2s regions for monolayer MoS_2 ribbons. (f) XPS spectra of the Na 1s region of the sapphire surface after reaction.

232.5 eV, corresponding to the double peaks of Mo $3d_{5/2}$ and Mo $3d_{3/2}$, respectively. The peak at 226.7 eV is attributed to S 2s. The results are consistent with the reported values of MoS_2 crystals [30–32]. In addition, the peak value of the Na 1s was detected on the surface of substrate as shown in Fig. 1f, indicating that Na compounds were generated in the reactant.

Two methods were used to investigate the single crystalline properties of the aligned MoS_2 ribbons. First, the ribbons were transferred onto the copper grid to conduct the TEM test. Fig. 2a shows the low-magnification TEM image of MoS_2 ribbons. Selected area electron diffraction (SAED) was further used to characterize the single crystal structure of MoS_2 ribbons. Four positions marked by 1, 2, 3 and 4 on the ribbon in Fig. 2a were selected. Fig. 2b–e show that the SAED patterns at these four positions. They all have six-fold symmetry and are completely coincident with no off-angle, indicating that the MoS_2 ribbon is a single crystal. Etching techniques have been widely used to detect the quality and crystallinity of 2D materials, especially for graphene and TMDC materials [33–35]. Yamamoto *et al.* [36] introduced oxygen treatment to MoS_2 thin films and found uniform orientation of triangular holes appearing on the surface of the thin film. Herein, a similar strategy was implemented to detect the crystallinity of the whole ribbon in the range of hundred microns from the orientation of etching pits. Samples were etched for 20 min at 500°C with 0.1% oxygen with 200 sccm. Fig. 2f shows the low-magnification SEM image of the ribbon after etching. The emergence of etching stripes is attributed to the large difference in thermal expansion coefficient between MoS_2 and sapphire [37]. The presence of strain reduces the stability of the ribbon and creates cracks under oxygen etching conditions. Fig. 2g reveals the high-magnification diagram of the red box area in Fig. 2f. The triangular etching holes remain in uniform orientation, indicating that the synthesized MoS_2 ribbon is a single crystal.

We also evaluated the electrical and optical properties of MoS_2 ribbons on the sapphire substrate. The electrical transports were measured by fabricating the Hall bar structure devices on the ribbon. As shown in Fig. 3a, the resistance of the Hall devices was plotted as a function of magnetic field, which was measured at 300 K, and the embedded diagram in Fig. 3a shows the device structure. The carrier mobility of the ribbon was obtained under the changing magnetic field from the standard Hall equation:

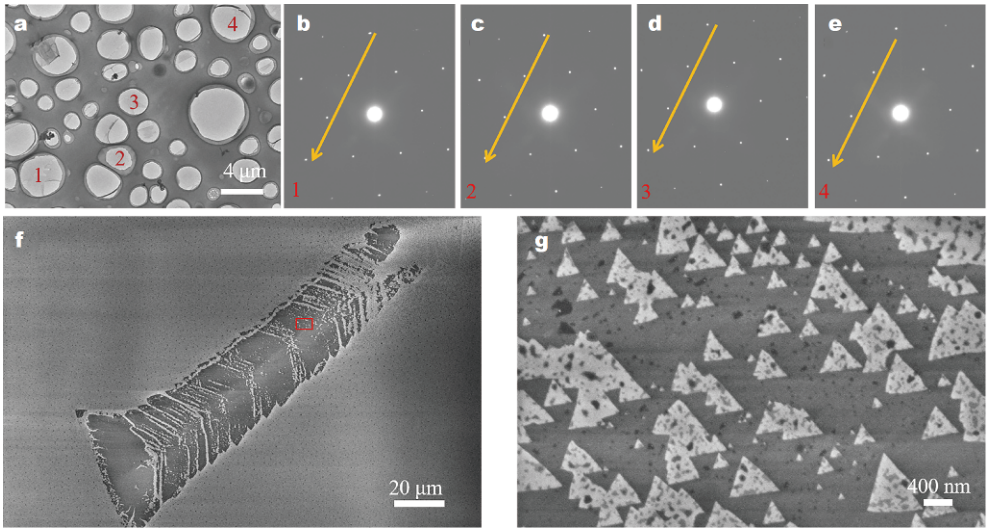

Figure 2 (a) Low-magnification TEM image of the MoS_2 ribbon. (b–e) Corresponding MoS_2 SAED patterns of different positions as marked by 1, 2, 3, 4 in Fig. 2a. (f) Low-magnification SEM images of monolayer MoS_2 ribbon after O_2 etching at 500°C. (g) High-magnification SEM images of the red box area in Fig. 2f, showing the triangular etching holes with uniform orientation.

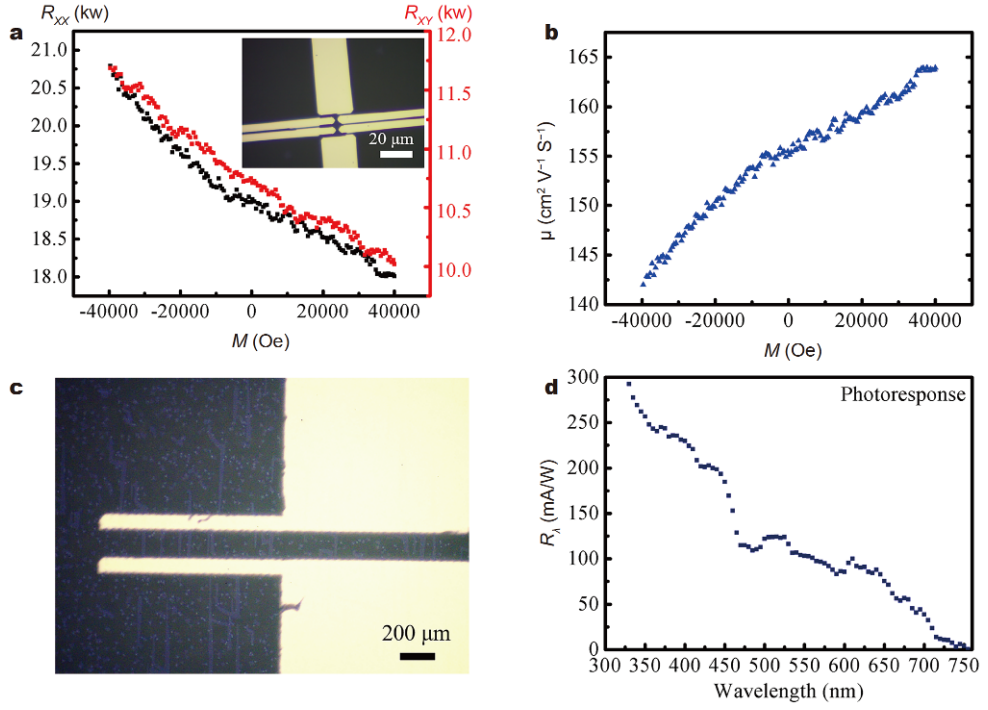

Figure 3 Evaluation of the electrical and optical properties of MoS_2 ribbons on sapphire. (a) Typical resistance of the MoS_2 Hall bar structure measured at 300 K under varying magnetic fields, where the inset shows an optical image of the device. (b) Carrier mobility of the ribbons under the changing magnetic field. (c) Optical image of the photoresponse device. (d) Photoresponsivity of the MoS_2 ribbon under different wavelengths.

$$\mu_{\text{hall}} = |R_{\text{H}}| * \sigma = \frac{1}{\beta} * \frac{L}{W} * \frac{R_{XY}}{R_{XX}}, \quad (1)$$

where R_{H} represents the Hall coefficient, σ is the electrical conductivity, β is the magnetic field, L is the length of channel, W represents the width of channel, R_{XY} is the Hall resistance, and R_{XX} is the longitude resistance. As

shown in Fig. 3b, the measured carrier mobility is approximately 150 $cm^2 V^{-1} s^{-1}$ at room temperature, indicating that the monolayer MoS_2 ribbon has a perfect electrical property. For the photodetector, the photoresponsivity (R) and the range of test spectra are important parameters that evaluate the ability of converting the light signals into electrical signals. R_λ is defined as

$$R_\lambda = \frac{I_{Ph}}{P_{light}}, \quad (2)$$

where $I_{ph} = I_{illumination} - I_{dark}$ is the photocurrent, P_{light} is the power of incident laser, and R_λ is the photoresponsivity measured in the unit of mA W^{-1}. Fig. 3c shows the device structure. The photoresponsivity values at different wavelengths calculated using the Equation (2) are shown in Fig. 3d. When the wavelength exceeded 750 nm, the photoresponsivity value was almost negligible because the incident energy was insufficient to stimulate the photon transition. When the wavelength was 550 nm, the photoresponsivity value was 103 mA W^{-1}, which was similar to the value reported in previous studies [38,39].

Mechanism of the VLS growth of MoS_2 ribbons

Effects of NaOH concentration on the morphology and orientation of MoS_2 ribbons

The amount of NaOH influenced the morphology and orientation of the MoS_2 ribbons. Fig. 4a–h are the optical

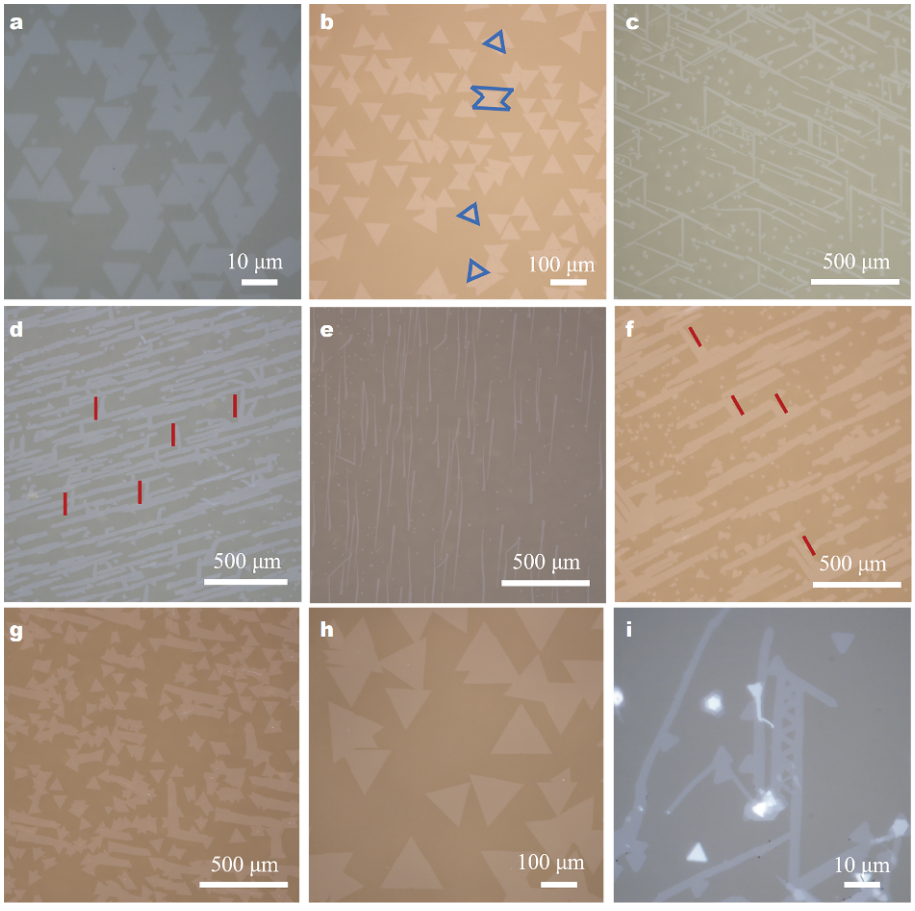

Figure 4 Changes in MoS_2 morphology and orientation with the increase in the amount of the introduced NaOH. (a) Without NaOH: oriented triangular MoS_2 domains with a size of 10 μm. (b) Very low NaOH content (1.5 mg): the size of triangular MoS_2 domains increased to 50 μm and appeared disordered, with the disordered domains marked by blue. (c) Low NaOH content (2.5 mg): oriented MoS_2 ribbons with the length of 300 μm. (d) More NaOH content (4 mg): aligned MoS_2 ribbons and a small fraction of disordered ribbons. (e) Increase in growth temperature: the majority of MoS_2 ribbons were aligned. (f) Continue to increase NaOH content (7 mg): proportion of aligned ribbons decreased and the width of the ribbons increased. Ribbons marked by red started to appear disordered. (g) Much more NaOH content (10 mg): disordered ribbons with their widths increased. (h) Excess NaOH content (14 mg): MoS_2 triangle with huge size and random directions. (i) The oriented MoS_2 ribbons on monolayer MoS_2 film.

images of MoS_2 ribbons grown with the increase in NaOH amount. Fig. 4a describes the triangular MoS_2 domains without the introduction of NaOH and the molybdenum-sulfur ratio is 5 mg:200 mg. The triangular MoS_2 epitaxially grows on the sapphire substrate and has a size of 10 μm. The dominant edge orientations are 0° and ±60° with the ratio of 1:1. The strong van der Waals interaction between MoS_2 and sapphire controlls the lattice orientation of MoS_2. In Fig. 4b, minimal amount of NaOH was introduced during the experiment. Before the growth process, 1.5 mg NaOH was mixed with 5 mg MoO_3 powders and kept other growth conditions unchanged. The morphology of MoS_2 remained triangular, but the MoS_2 domains had considerable breakthrough in size. Alkali metal cations can promote the lateral growth of MoS_2. The majority of single crystal MoS_2 remained oriented on the substrate, but a small fraction of domains appeared disordered as marked by blue in Fig. 4b. When the NaOH content was increased (2.5 mg NaOH and 5 mg MoO_3), the oriented MoS_2 ribbons appeared on the substrate, as shown in Fig. 4c. The ribbons exhibited three main directions on the substrate with a ratio of 1:1:1, and the included angle was 120° or 60°. Additional characterizations are shown in the Supplementary information (Fig. S1). In Fig. 4d, as the NaOH content continued to increase (4 mg NaOH and 5 mg MoO_3), the arrangement of MoS_2 ribbons changed from oriented to aligned on the sapphire. Only a few ribbons marked with red lines arranged in other directions. As shown in Fig. 4e, a large range of aligned MoS_2 ribbons were obtained by increasing the growth temperature. In Fig. 4f, when higher amount of NaOH was introduced to the reaction (7 mg NaOH and 5 mg MoO_3), the proportion of aligned ribbons decreased and the width of the ribbons increased. In local area, some ribbons marked by red started to appear disordered. In Fig. 4g, the number of ribbons decreased and they exhibited random directions when the NaOH content continued to increase (10 mg NaOH and 5 mg MoO_3). In Fig. 4h, when the NaOH content was excessive (14 mg NaOH and 5 mg MoO_3), only large triangular MoS_2 domains and continuous films were obtained on the sapphire. The size of triangular MoS_2 domains was up to 100 μm, but they exhibited random directions. As shown in Fig. 4i, the oriented monolayer MoS_2 ribbons could also be acquired on the MoS_2 continuous films in the sample of Fig. 4h; their predominant growth directions were 60° or 120°. SEM, AFM, and Raman characterization results are shown in Fig. S2. Li *et al.* [28] found that the oriented ribbons were induced by the orientation of the underlying MoS_2 crystal.

Interaction between MoS_2 and sapphire

PL and Raman spectra were conducted under different amounts of NaOH to determine the growth mechanism of MoS_2 ribbons *via* the NaOH-assisted CVD. The strain in MoS_2 ribbons and the interaction with the substrate were analyzed by comparing the shifts in peaks of PL and Raman spectra.

As shown in Fig. 5a, the PL spectra of MoS_2 were obtained at room temperature. With regard to the oriented triangular MoS_2 domains obtained without the introduction of NaOH in Fig. 4a, an A-exciton peak at 1.88 eV was observed. This peak is the typical PL peak position of CVD-grown MoS_2. By comparison, the PL

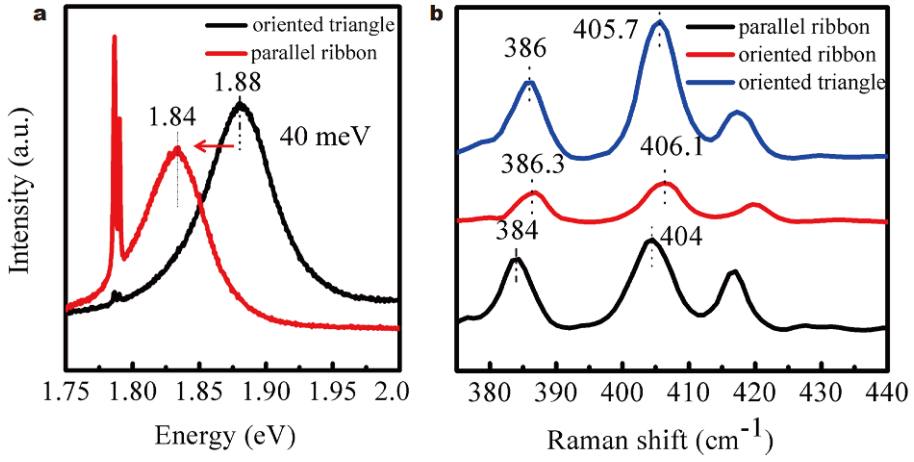

Figure 5 PL and Raman characterizations of MoS_2 ribbons and triangles. (a) The PL spectra of aligned MoS_2 ribbons show red shift when NaOH was introduced. (b) Comparison of Raman spectra between MoS_2 ribbons and triangles. The spectra of oriented triangle, oriented ribbon, and aligned ribbon are shown by blue, red, and black curves, respectively.

peak of the aligned MoS_2 ribbons in Fig. 4e shows a red shift of 40 meV. Liu *et al.* [40] systematically characterized the CVD-grown MoS_2 by PL spectroscopy and revealed that the tensile strain in MoS_2 domains can be identified by the shifting of PL peak. Density functional theory (DFT) calculations also established the linear relationship between the PL peak shifting and the strain variations in MoS_2, and the linear coefficient was approximately −44 meV per % strain (negative sign indicates redshift). Conley *et al.* [7] and Castellanos-Gomez *et al.* [41] measured the linear coefficients between the PL peak shifting and strain in MoS_2 and found that they were about −45 and −36 meV per % strain, respectively. According to the above calculation and experimental results reported previously, the aligned monolayer MoS_2 ribbons possibly suffered from approximately 1% tensile strain compared with oriented triangles.

E_{2g}^1 and A_{1g} are the two main active modes in Raman spectra of MoS_2. E_{2g}^1 mode corresponds to the in-plane vibration and A_{1g} represents the out-of-plane lattice expansion [42]. The two vibration modes provide the information on the strain in the samples and the strength of van der Waals interaction between MoS_2 and the substrate. Raman characterizations of the oriented triangular MoS_2 domain, oriented MoS_2 ribbon and aligned MoS_2 ribbon in Fig. 4a, c, e were conducted. The results are shown in black, red, and blue curves in Fig. 5b.

Comparison of the blue and red curves indicated very small difference in the position of Raman characteristic peaks between the oriented MoS_2 ribbons and the oriented triangular MoS_2 domains, revealing that MoS_2 suffered from the consistent strain in both cases. In Fig. 5b, a red shift of E_{2g}^1 from 386 cm^{-1} to 384 cm^{-1} occurs, by comparing the blue and black curves. When tensile strain was applied to monolayer MoS_2, the E_{2g}^1 mode would experience red shift or even split [43]. The red shift of E_{2g}^1 suggests that the aligned MoS_2 ribbons suffered from considerable tensile strain, which may be caused by the thermal and lattice mismatch between MoS_2 and the sapphire substrate. Rice *et al.* [44] linearly fitted the relationship between the peak position shifting and strain based on DFT, and found that the red-shift coefficient of monolayer MoS_2 E_{2g}^1 mode was −2.1 cm^{-1} per % strain. Wang *et al.* [45] conducted micro-Raman spectroscopy of MoS_2 on flexible matrix polyethylene terephthalate under controllable uniaxial tensile strain, and confirmed this linear results. In Fig. 5b, the peak of the aligned monolayer MoS_2 ribbon shows a red shift of 2 cm^{-1}, which is subjected to 1% tensile strain. The results of Raman and PL are consistent, further verifying the tensile strain in the aligned MoS_2 ribbons.

Zhou *et al.* [46] suggested that the out-of-plane Raman vibration depended on the interactions with the adjacent material; the shift of A_{1g} showed the strength of the van der Waals interaction between MoS_2 and the substrate. As shown in Fig. 5b, A_{1g} displays red shifts from 405.7, 406.1 to 404 cm^{-1} by comparing the blue, red and the black curves. We concluded that the oriented triangular MoS_2 domains in Fig. 4a and the oriented MoS_2 ribbons in Fig. 4c exhibited stronger van der Waals interactions with the substrate. By contrast, the aligned MoS_2 ribbons showed weak van der Waals interaction with the sapphire. The weakening of the interaction should be related to the changes in MoS_2 shape and orientation.

Growth models of aligned MoS_2 ribbons

Without NaOH, the CVD growth of MoS_2 exhibited a typical VSS growth mode. S and MoO_3 are transported through the gas phase to the surface of the sapphire substrate to form atomic-level monolayer MoS_2 clusters [9]. The MoS_2 clusters maintain a certain degree of rotation/translation with respect to the surface due to the weak van der Waals interaction with the substrate at the initial stage of growth [47]. In the end, those clusters are pinned down in the most stable orientation with the substrate when they reach a certain size. As shown on the left side of Fig. 6a, the triangular MoS_2 domains exhibit two preferential orientations of 0° and 60° parallel to the sapphire substrate direction [11−20].

The introduction of NaOH causes the growth mechanism to transfer to VLS deposition. A possible reaction route is as follows:

$$MoO_3 + 2NaOH \rightarrow Na_2MoO_4\ (L) + H_2O, \quad (3)$$

$$Na_2MoO_4\ (L) + 5S \rightarrow MoS_2 + Na_2S + 2SO_2. \quad (4)$$

MoS_2 ribbons form on the substrate when the Na_2MoO_4 droplets crawl on the surface [9]. The assistance of Na^+ reduces the reaction energy required for the generation of MoS_2 [24,20]. The MoS_2 clusters grow rapidly, and not enough time is available to adjust the orientation relationship with the sapphire substrate like in the VSS mode. Consequently, the original epitaxial relationship between MoS_2 and the sapphire substrate is broken. The introduction of NaOH offsets the most stable arrangement of MoS_2 on the substrate so as to change the interactions with sapphire, resulting in the shifts of Raman and PL characteristic peaks.

The orientation of MoS_2 ribbons on C-plane sapphire can be divided into two cases, namely, oriented and aligned arrangement. In the first case, the MoS_2 ribbons are oriented on the substrate in three directions with an

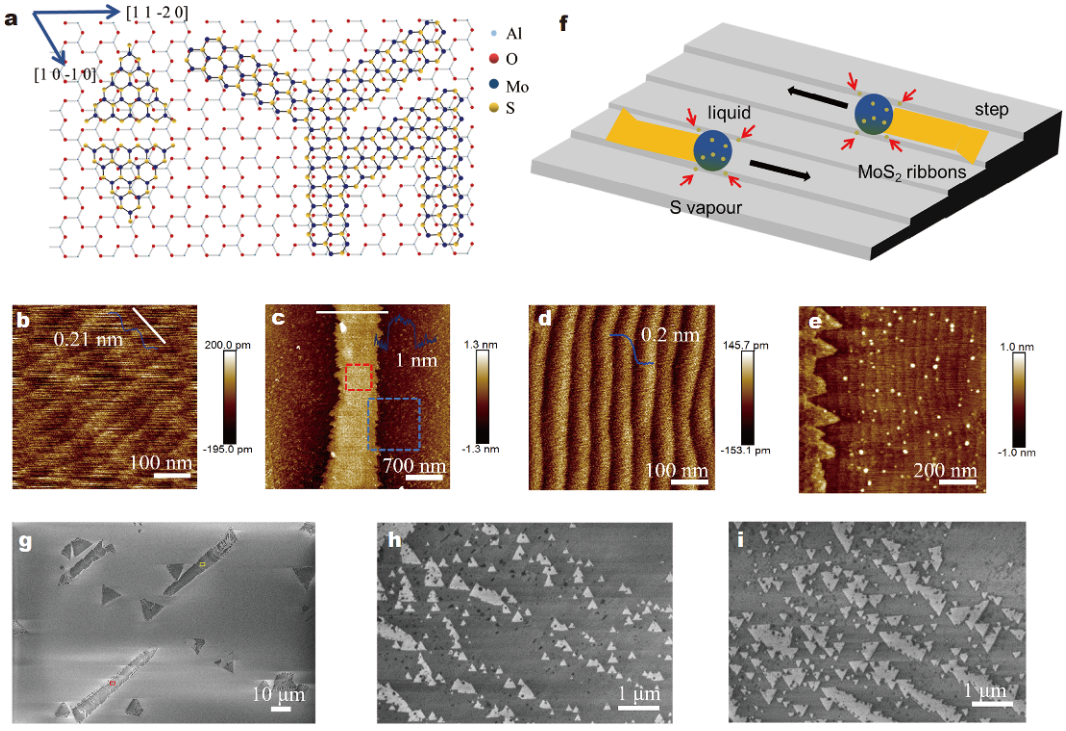

Figure 6 Growth models of MoS_2 ribbons. (a) Schematic diagram of epitaxial growth of oriented triangular MoS_2 domains and ribbons on the (0001) surface of sapphire. (b) Atomic steps on the sapphire substrate. (c) AFM image of the aligned MoS_2 ribbons with small width. The thickness of the ribbon is 1 nm. (d) AFM image of the red box area, showing the atomic steps on the MoS_2 ribbons. (e) AFM image of surface morphology at the junction of MoS_2 ribbons and substrate marked by blue box in (c). (f) Growth schematic diagram of the aligned MoS_2 ribbons. (g) Low-magnification SEM image of bi-directional MoS_2 ribbons after oxygen etching. (h) High-magnification SEM image of the red box area in (g), showing the oxygen etching holes with upward direction. (i) High-magnification SEM image of the yellow box area in (g), showing the downward oxygen etching holes. The bars in (b–d) are the height profiles plotted along the white lines.

included angle of 60° or 120°, as shown in Fig. 4c. The diagram of the oriented MoS_2 ribbons on the (0001) surface of sapphire is given on the right side of Fig. 6a. Compared with the arrangement of the oriented triangular MoS_2 domains, the growth directions of the ribbons are along the center to the vertex of triangular MoS_2, and the angles between the ribbons and the sapphire [11−20] direction are ±30° and 90°. This result is determined by the mechanism of the crystal growth. The CVD growth of MoS_2 is a typical anisotropic growth. MoS_2 grows fast in these three directions, and thus the ribbons are oriented in these three directions. Regardless of the oriented MoS_2 ribbons or oriented triangular MoS_2 domains on sapphire, the oriented growth is determined by a single epitaxial relationship between the sapphire and MoS_2 in the strongest direction. The small lattice mismatch and the van der Waals interaction between MoS_2 and the sapphire play key roles. Similar to the growth of tin-doped indium oxide (ITO) nanowires on yttria-stabilized zirconia substrate reported by Shen *et al.* [48], in the gold nanoparticle-catalyzed VLS growth mode, the growth direction and crystallization orientation of ITO were affected by the epitaxial relationship between nanowires and substrate.

In the second case, the MoS_2 ribbons are aligned on the sapphire substrate. We focused on the growth mechanism of the aligned MoS_2 ribbons in this case. To eliminate the influence of airflow on the directions of the synthesized MoS_2 ribbons, we adjusted the angle between the airflow and substrate during growth. However, we found that the MoS_2 ribbons still grew in a fixed direction on the substrate. Thus, this determined aligned growth direction was controlled by the sapphire substrate itself. More details are shown in Fig. S3.

AFM was used to characterize the surface of the C-plane sapphire. The surface morphology image of a 1 μm × 1 μm area is shown in Fig. 6b. The surface shows steps due to the small miscut induced during the cutting of the sapphire boule [49]. The step height is about 0.21 nm and the width is 70 nm. Fig. 6c is a typical AFM height image

of the MoS_2 ribbon. The thickness of the ribbon is 1 nm, indicating a monolayer MoS_2 ribbon. Fig. 6d shows the surface morphology of a 1 μm × 1 μm area marked by red box in Fig. 6c. The surface is atomically flat with atomic steps because the MoS_2 ribbon replicates the step structures inherent in sapphire. Most importantly, we found that the step direction was parallel to the direction of the MoS_2 ribbon. To explore this orientation relationship, the surface morphology at the junction of MoS_2 ribbon and the substrate marked by blue box in Fig. 6c was also characterized. As shown in Fig. 6e, the direction of the steps on the substrate, the direction of MoS_2 ribbons and the step direction on the surface of MoS_2 ribbons are completely parallel. To visualize this parallel relationship, we selected a small-width MoS_2 ribbon for measurement and different widths of ribbons were measured as shown in Fig. S4. Therefore, the growth of the aligned ribbons along the sapphire step was proved to be universal. The formation mechanism of the aligned MoS_2 ribbons was mainly related to the guiding effect of the C-plane sapphire surface steps caused by miscut.

The schematic growth diagram of the aligned ribbons is given in Fig. 6f. The competition between lattice-directed and nanostep directed modes during single-walled carbon nanotube (SWNT) growth has been observed on both sapphire and quartz substrates [50,51]. Owing to the introduction of the increased amounts of NaOH, the fluidity of Na_2MoO_4 droplet was further enhanced, resulting in rapid crawling of the droplets along the steps. When S vapor were dissolved into the Na_2MoO_4 droplets until saturation, MoS_2 clusters were precipitated at the steps and MoS_2 ribbons grew along the steps. However, in the direction perpendicular to the step, the energy required for growing across the step was higher and the growth rate was slower than growing along the step direction [52]. With the increase in the amount of the introduced NaOH, the van der Waals interaction between MoS_2 and sapphire became weaker. Nanostep directed mode was dominant, and the guided growth of MoS_2 ribbons changed from six directions to bi-directions. Thus, step-guided ribbons were obtained. The cooperation and competition between the two modes resulted in the disordered ribbons in Fig. 4d, f. David *et al.* [53] reported the VLS growth of aligned GaN nanowires on different sapphire planes by introducing nanosteps, which was named as the graphoepitaxial effect. The growth mechanism of aligned MoS_2 ribbons is similar to the graphoepitaxial effect. The existence of steps breaks the van der Waals epitaxial relationship between MoS_2 and sapphire, which can induce the ribbons to grow with different epitaxial relationships and crystallizations.

We found that the growth direction of the adjacent ribbons was in opposite directions. Additional characterizations are shown in Fig. S5. Oxygen etching was performed to detect the orientation relationship of the two adjacent MoS_2 ribbons. Fig. 6g is the low-magnification SEM image of the aligned ribbons after oxygen etching. Fig. 6h, i are the high-magnification SEM images of red and yellow box areas in Fig. 6g, respectively. The direction of etching holes in these two areas are opposite with a difference of 180°, suggesting that the orientation relationship between the two adjacent MoS_2 ribbons is similar to that of oriented triangular MoS_2 domains with the orientation of 0° and 60°. In addition, MoS_2 nanoribbons are not obtained on the sapphire substrate. A possible reason is that the introduction of NaOH enhances the lateral growth speed of MoS_2. The eutectic intermediate containing alkali molybdate and molybdenum oxides has a low melting point, which could facilitate their mobility and lateral growth [21], weakening the epitaxial control from substrate and graphoepitaxial guide from surface steps. Thus, the triangular MoS_2 domains with large size and random arrangements were obtained when a large amount of NaOH was introduced.

CONCLUSION

In summary, we successfully prepared MoS_2 ribbons on sapphire substrates *via* the NaOH-assisted CVD method. The amount of the introduced NaOH played an important role in controlling the morphology and orientation of MoS_2. This process can realize continuous adjustment from oriented triangular domains to oriented MoS_2 ribbons induced by van der Waals interaction, and to aligned MoS_2 ribbons induced by surface steps and large-sized triangular MoS_2 domains. The aligned MoS_2 ribbons have high electronic mobility and perfect optical response. The possible growth mechanism of the aligned MoS_2 ribbons was also analyzed. Our work advances the fundamental research on MoS_2 ribbons and their applications in electronics and optoelectronic devices. The present study also propels the realization of an array of devices.

Received 22 December 2019; accepted 10 February 2020; published online 27 March 2020

1 Radisavljevic B, Radenovic A, Brivio J, *et al.* Single-layer MoS_2 transistors. Nat Nanotech, 2011, 6: 147–150
2 Wang QH, Kalantar-Zadeh K, Kis A, *et al.* Electronics and optoelectronics of two-dimensional transition metal dichalcogenides. Nat Nanotech, 2012, 7: 699–712

3 Mak KF, Lee C, Hone J, *et al.* Atomically thin MoS_2: A new direct-gap semiconductor. Phys Rev Lett, 2010, 105: 136805
4 Khan MF, Iqbal MW, Iqbal MZ, *et al.* Photocurrent response of MoS_2 field-effect transistor by deep ultraviolet light in atmospheric and N_2 gas environments. ACS Appl Mater Interfaces, 2014, 6: 21645–21651
5 Zeng H, Dai J, Yao W, *et al.* Valley polarization in MoS_2 monolayers by optical pumping. Nat Nanotech, 2012, 7: 490–493
6 Mak KF, He K, Shan J, *et al.* Control of valley polarization in monolayer MoS_2 by optical helicity. Nat Nanotech, 2012, 7: 494–498
7 Conley HJ, Wang B, Ziegler JI, *et al.* Bandgap engineering of strained monolayer and bilayer MoS_2. Nano Lett, 2013, 13: 3626–3630
8 Zhang X, Nan H, Xiao S, *et al.* Shape-uniform, high-quality monolayered MoS_2 crystals for gate-tunable photoluminescence. ACS Appl Mater Interfaces, 2017, 9: 42121–42130
9 Zhu D, Shu H, Jiang F, *et al.* Capture the growth kinetics of CVD growth of two-dimensional MoS_2. npj 2D Mater Appl, 2017, 1: 8
10 Yang X, Li Q, Hu G, *et al.* Controlled synthesis of high-quality crystals of monolayer MoS_2 for nanoelectronic device application. Sci China Mater, 2016, 59: 182–190
11 Fang M, Wang F, Han Y, *et al.* Controlled growth of bilayer-MoS_2 films and MoS_2-based field-effect transistor (FET) performance optimization. Adv Electron Mater, 2018, 4: 1700524
12 Li Z, Liu C, Rong X, *et al.* Tailoring MoS_2 valley-polarized photoluminescence with super chiral near-field. Adv Mater, 2018, 30: 1801908
13 Liu S, Yin Y, Wu M, *et al.* Phosphorus-mediated MoS_2 nanowires as a high-performance electrode material for quasi-solid-state sodium-ion intercalation supercapacitors. Small, 2019, 15: 1900524
14 Xu H, Zhang H, Guo Z, *et al.* High-performance wafer-scale MoS_2 transistors toward practical application. Small, 2018, 14: 1803465
15 Liu HF, Wong SL, Chi DZ. CVD growth of MoS_2-based two-dimensional materials. Chem Vap Deposition, 2015, 21: 241–259
16 Cai Z, Liu B, Zou X, *et al.* Chemical vapor deposition growth and applications of two-dimensional materials and their heterostructures. Chem Rev, 2018, 118: 6091–6133
17 Najmaei S, Liu Z, Zhou W, *et al.* Vapour phase growth and grain boundary structure of molybdenum disulphide atomic layers. Nat Mater, 2013, 12: 754–759
18 Rhyee JS, Kwon J, Dak P, *et al.* High-mobility transistors based on large-area and highly crystalline CVD-grown $MoSe_2$ films on insulating substrates. Adv Mater, 2016, 28: 2316–2321
19 Nie Y, Liang C, Zhang K, *et al.* First principles kinetic Monte Carlo study on the growth patterns of monolayer WSe_2. 2D Mater, 2016, 3: 025029
20 Song JG, Hee Ryu G, Kim Y, *et al.* Catalytic chemical vapor deposition of large-area uniform two-dimensional molybdenum disulfide using sodium chloride. Nanotechnology, 2017, 28: 465103
21 Wang P, Lei J, Qu J, *et al.* Mechanism of alkali metal compound-promoted growth of monolayer MoS_2: Eutectic intermediates. Chem Mater, 2019, 31: 873–880
22 Kim H, Han GH, Yun SJ, *et al.* Role of alkali metal promoter in enhancing lateral growth of monolayer transition metal dichalcogenides. Nanotechnology, 2017, 28: 36LT01
23 Zhu J, Xu H, Zou G, *et al.* MoS_2–OH bilayer-mediated growth of inch-sized monolayer MoS_2 on arbitrary substrates. J Am Chem Soc, 2019, 141: 5392–5401
24 Wang Z, Xie Y, Wang H, *et al.* NaCl-assisted one-step growth of MoS_2–WS_2 in-plane heterostructures. Nanotechnology, 2017, 28: 325602
25 Yun SJ, Han GH, Kim H, *et al.* Telluriding monolayer MoS_2 and WS_2 *via* alkali metal scooter. Nat Commun, 2017, 8: 2163
26 Zhou J, Lin J, Huang X, *et al.* A library of atomically thin metal chalcogenides. Nature, 2018, 556: 355–359
27 Yang P, Zou X, Zhang Z, *et al.* Batch production of 6-inch uniform monolayer molybdenum disulfide catalyzed by sodium in glass. Nat Commun, 2018, 9: 979
28 Li S, Lin YC, Zhao W, *et al.* Vapour–liquid–solid growth of monolayer MoS_2 nanoribbons. Nat Mater, 2018, 17: 535–542
29 Chen T, Hao G, Wang G, *et al.* Controlled growth of atomically thin $MoSe_2$ films and nanoribbons by chemical vapor deposition. 2D Mater, 2019, 6: 025002
30 Song JG, Ryu GH, Lee SJ, *et al.* Controllable synthesis of molybdenum tungsten disulfide alloy for vertically composition-controlled multilayer. Nat Commun, 2015, 6: 7817
31 Liu KK, Zhang W, Lee YH, *et al.* Growth of large-area and highly crystalline MoS_2 thin layers on insulating substrates. Nano Lett, 2012, 12: 1538–1544
32 Zhang J, Yu H, Chen W, *et al.* Scalable growth of high-quality polycrystalline MoS_2 monolayers on SiO_2 with tunable grain sizes. ACS Nano, 2014, 8: 6024–6030
33 Ly TH, Duong DL, Ta QH, *et al.* Nondestructive characterization of graphene defects. Adv Funct Mater, 2013, 23: 5183–5189
34 Zhang Y, Zhang H, Li F, *et al.* Invisible growth of microstructural defects in graphene chemical vapor deposition on copper foil. Carbon, 2016, 96: 237–242
35 Zhang Y, Zhang Y, Ji Q, *et al.* Controlled growth of high-quality monolayer WS_2 layers on sapphire and imaging its grain boundary. ACS Nano, 2013, 7: 8963–8971
36 Yamamoto M, Einstein TL, Fuhrer MS, *et al.* Anisotropic etching of atomically thin MoS_2. J Phys Chem C, 2013, 117: 25643–25649
37 Wu D, Huang H, Zhu X, *et al.* Raman mode in thermal strain-fractured CVD-MoS_2. Crystals, 2016, 6: 151
38 Zhang Q, Pang W, Sun C, *et al.* Molybdenum disulfide photodetector based on field effect transistor. Nanotechnology & Precision Engineering, 2016, 14: 360–364
39 Xie Y, Zhang B, Wang S, *et al.* Ultrabroadband MoS_2 photodetector with spectral response from 445 to 2717 nm. Adv Mater, 2017, 29: 1605972
40 Liu Z, Amani M, Najmaei S, *et al.* Strain and structure heterogeneity in MoS_2 atomic layers grown by chemical vapour deposition. Nat Commun, 2014, 5: 5246
41 Castellanos-Gomez A, Roldán R, Cappelluti E, *et al.* Local strain engineering in atomically thin MoS_2. Nano Lett, 2013, 13: 5361–5366
42 Zhang X, Qiao XF, Shi W, *et al.* Phonon and Raman scattering of two-dimensional transition metal dichalcogenides from monolayer, multilayer to bulk material. Chem Soc Rev, 2015, 44: 2757–2785
43 Lloyd D, Liu X, Christopher JW, *et al.* Band gap engineering with ultralarge biaxial strains in suspended monolayer MoS_2. Nano Lett, 2016, 16: 5836–5841
44 Rice C, Young RJ, Zan R, *et al.* Raman-scattering measurements and first-principles calculations of strain-induced phonon shifts in monolayer MoS_2. Phys Rev B, 2013, 87: 081307
45 Wang Y, Cong C, Qiu C, *et al.* Raman spectroscopy study of lattice vibration and crystallographic orientation of monolayer MoS_2 under uniaxial strain. Small, 2013, 9: 2857–2861

46 Zhou KG, Withers F, Cao Y, *et al.* Raman modes of MoS_2 used as fingerprint of van der Waals interactions in 2-D crystal-based heterostructures. ACS Nano, 2014, 8: 9914–9924
47 Dumcenco D, Ovchinnikov D, Marinov K, *et al.* Large-area epitaxial monolayer MoS_2. ACS Nano, 2015, 9: 4611–4620
48 Shen Y, Turner S, Yang P, *et al.* Epitaxy-enabled vapor–liquid–solid growth of tin-doped indium oxide nanowires with controlled orientations. Nano Lett, 2014, 14: 4342–4351
49 Curiotto S, Chatain D. Surface morphology and composition of c-, a- and m-sapphire surfaces in O_2 and H_2 environments. Surf Sci, 2009, 603: 2688–2697
50 Ago H, Imamoto K, Ishigami N, *et al.* Competition and cooperation between lattice-oriented growth and step-templated growth of aligned carbon nanotubes on sapphire. Appl Phys Lett, 2007, 90: 123112
51 Li P, Zhang J. Preparation of horizontal single-walled carbon nanotubes arrays. Top Curr Chem (Z), 2016, 374: 85
52 Xiao J, Dunham S, Liu P, *et al.* Alignment controlled growth of single-walled carbon nanotubes on quartz substrates. Nano Lett, 2009, 9: 4311–4319
53 Tsivion D, Schvartzman M, Popovitz-Biro R, *et al.* Guided growth of millimeter-long horizontal nanowires with controlled orientations. Science, 2011, 333: 1003–1007

Acknowledgements This work was financially supported by the Science and Technology Commission of Shanghai Municipality (18511110700). The synthesis was sponsored by the State Key Laboratory of Functional Materials for Informatics. Materials characterization was conducted at the CAS Center of Excellence in Superconducting Electronics.

Author contributions Hu S and Yu G designed the experiments. Li J and Hu S grew the MoS_2 samples. Chen Z carried out the transfer of MoS_2. Zhan X carried out the XPS testing. Sui Y and Wang S performed the Raman characterizations of all samples and analysis. Kang H performed the AFM characterization of the samples. Liang Y performed the SEM testing. Peng S, Jin Z, Liu X measured the PL property in MoS_2. Jiang D and Lei L fabricated the Hall bar structure device. Hu S designed the MoS_2 photodetector devices. Hu S and Li J wrote the paper. All authors discussed and commented on the manuscript. The manuscript was written through contributions of all authors. All authors have given approval to the final version of the manuscript.

Conflict of interest The authors declare no conflict of interest.

Supplementary information Supporting data are available in the online version of the paper.

Shike Hu is a master student under the guidance of Prof. Guanghui Yu at Shanghai Institute of Microsystem and Information Technology, Chinese Academy of Sciences, China. She received her BSc degree at the School of Optical and Electronic Information, Huazhong University of Science and Technology in 2015. Her current research concentrates on the growth of 2D materials and their applications in nano electronics.

Jing Li is a master student under the guidance of Prof. Guanghui Yu at Shanghai Institute of Microsystem and Information Technology, Chinese Academy of Sciences, China. He received his BSc degree from the School of Materials Science and Engineering, China University of Mining and Technology in 2016. His current scientific interest focuses on the special growing phenomena and electronics of 2D materials and heterostructures.

Guanghui Yu received his BSc degree from Jilin University. He obtained his PhD degree from Changchun Institute of Physics, Chinese Academy of Sciences in 1999. Then he worked as a postdoctoral fellow at Chiba University, Japan (1999–2002). He is currently a professor and has been a group leader at Shanghai Institute of Microsystem and Information Technology, Chinese Academy of Sciences since 2002. His current research interest includes the controlled growth and application exploration of 2D crystals.

蓝宝石衬底上NaOH辅助CVD法制备有序单层MoS_2条带

胡诗珂[1,2†], 李晶[1,2†], 展肖依[1,2], 王爽[1,2], 雷龙彪[1,2], 梁逸俭[1,2], 康鹤[1,2], 张燕辉[1], 陈志鎏[1], 隋妍萍[1], 姜达[1], 于广辉[1,2*], 彭松昂[3], 金志[3], 刘新宇[3]

摘要 本文报道了一种在蓝宝石衬底上NaOH辅助化学气相沉积(CVD)生长有序排列单层MoS_2条带的方法. MoS_2条带具有优良的单晶性, 其载流子迁移率为~150 $cm^2 V^{-1} s^{-1}$, 在550 nm波长下的光学响应为103 mA W^{-1}. 单层MoS_2条带在蓝宝石衬底上具有两种生长方式, 其中一种为受层间范德华力以及晶格影响的取向生长, 另一种为受蓝宝石台阶约束的平行生长. NaOH的引入量对MoS_2形态与取向起重要作用, 可以实现从取向性三角形晶畴, 受衬底晶格影响的取向MoS_2条带, 受衬底台阶约束的平行条带, 再到大尺寸杂乱取向三角形晶畴的连续可调. 本文的结果有利于推动MoS_2的基础研究及器件应用, 也为合成其他一维和二维纳米结构开辟了新途径.

